Article

Understanding the Stability of Hollow Nanoparticles with Polycrystalline Shells

Felipe J. Valencia,* Max Ramírez, Alejandro Varas, and José Rogan

Read Online

ACCESS | Metrics & More | Article Recommendations | Supporting Information

ABSTRACT: The existence of polycrystalline shells has been widely reported in the synthesis of hollow nanoparticles; however, the exact role displayed by the grain boundaries on the stability has been scarcely studied. By including them, in this work, we study for the first time the contribution of the polycrystalline structure in the stability of this unique kind of nanostructures, addressing at the same time, a more realistic modeling of hollow nanoparticles. The role of the polycrystalline structure was studied in gold hollow nanoparticles using molecular dynamics simulations for a wide range of shell thickness and grain sizes. One of the main findings is that the shell thickness necessary for transition from a spherical to a shrunk structure is related to the grain size reduction. The results suggest that to achieve larger hollow nanoparticles, less defective shells are necessary, with single-crystal shells establishing an upper limit in the size that a structure can attain. The cavity shrinkage in a polycrystalline HNP is due to a complex combination of grain diffusion, rotations, dislocation emission, and twining, all of them activated from the grain boundary regions. Our findings suggest that the polycrystalline structure is a crucial parameter to control and improve the stability of the hollow nanoparticles.
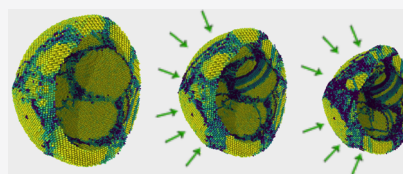
INTRODUCTION

Since the synthesis of the first hollow nanoparticle (hNP), the development in the field has been massive. Fueled by the remarkable performance in areas such as catalysis,[1] plasmonics,[2] sensing,[3] and energy storage,[4,5] among others,[6] studies have traced several synthesis routes in order to control the hNP size, thickness, and shape.[7−11] In fact, hNPs can be synthesized from metals, oxides, ceramics, or even from polymers, with sizes ranging from few to hundred nanometers.[12−16] Furthermore, the importance of maximizing the hNP size while decreasing the shell thickness is an alternative not only to produce lower cost and lightweight devices but also to improve their performance for storage, diffusion, or other surface-activated processes.[15,17,18]

Unlike conventional non-hNPs, the cavity of hNPs introduces surface effects that compromise their structural stability. In practice, it could be possible that some combination of radius and thickness was not potentially synthesizable, or in its defect, highly unstable, and therefore, with poor performance for practical applications. While structural characterizations are often conducted by transmission electron microscopy or X-ray diffraction techniques,[19] the dominant atomistic mechanisms involved in the stability of hNPs are still challenging to identify. Complementary, molecular dynamics (MD) simulations offer valuable information about the forces and atomistic-scale mechanisms that govern the hNP stability.[20−24] The first contribution employing MD simulations was made by Jiang *et al.*[24] in Au hNPs; their work highlight that an Au hNP with a relatively large diameter in comparison with their thickness tends to be unstable or collapse even at room conditions. Lately,

Akbarzadeh *et al.*[25,26] discuss the role of dominant surface effects, while Reyes *et al.*[23] note that metallic hNPs with lower stacking fault (SF) energy are prone to the structural collapse.

To the best of our knowledge, all the available atomistic studies of thermal and mechanical stability[15,20,26−30] consider single-crystal hNPs, something difficult to obtain under realistic experimental conditions. In fact, for single-crystal hNPs, the failure is triggered by the slips of preferential planes due to surface stresses,[23,24] in the absence of other plasticity sources, and the stability of pristine samples can be idealized. During the synthesis of hNPs, techniques such as calcination,[11,31] Kirkendall effect,[7,32] or laser ablations[33,34] tend to produce channels and fractures on the hNP shell during the template removal. Therefore, once the hNP is synthesized, it is expected to have irregularities as polycrystalline domains or porous shells.[1,2,7,35−40] Notwithstanding, none of these factors have been discussed as a potential collapse mechanism.

We note that to obtain ultrathin hNPs, several methods and post-synthesis techniques have been conducted.[15,17,18,41] The minimum shell thicknesses reported by experiments[38−40] are often larger than those reported from MD simulations[24,28,29] of single-crystal hNPs; however, MD predicts thickness of a few lattice parameters, with a well-defined failure mechanism.[23]
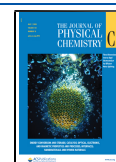
The major differences would be on the preexistence of defects, which are commonly observed during the synthesis process. Although experiments can be less invasive with the templates, the limit of the thickness that a hNP can attain is limited by mechanical effects, which could strongly affect the presence of polycrystalline domains.[32,42]

Thus, the investigation presented here is focused on the study of structural stability of hNPs with defects, in particular, in hNPs with polycrystalline shells as a more realistic approach to the modeling of hNPs. Among all possible materials to study the stability of hNPs, we chose gold because of experimental evidence showing its grain boundary structure,[2,36−40] and the available atomistic simulations that study the hNP with single-crystal shells.[24] We performed MD simulations over a wide range of size, shell thickness, and different grain boundary densities, in order to understand how a defective structure limit the stability and performance of hNPs under different scenarios.

■ METHODS

In order to analyze the structural stability of polycrystalline Au hNPs, we performed MD simulations using the LAMMPS code.[43] The interatomic interaction between Au atoms is modeled using the embedded atom method (EAM) potential,[44] with the parameters by Sheng et al.[45] MD simulations, along with the EAM potential has been successfully applied to various systems, reproducing experimental and density functional theory calculations of elastic constants,[46] formation energies,[47] SF, and twin energies,[48] among other properties. All these parameters constitute relevant information for the study of Au hNPs.

Each hNP, with a desired radius and thickness (t), was made by carving up a polycrystalline Au sample, with a specific average grain size (d), which is controlled through a Voronoi tessellation algorithm.[49,50] To avoid high energy grain boundaries or atom overlapping, we removed from the sample all the atoms with energies higher than 50 eV, principally from the grain boundary interface; then, we relaxed the polycrystal by using a conjugate gradient method coupled with a box relaxation algorithm. Also, to allow grain boundary re-accommodation, and to circumvent spurious effects due to high energy grain boundaries, we annealed the sample at a temperature of $T = 2T_m/3$, where T_m is the Au melting point. The system temperature is controlled using a Nose−Hoover algorithm coupled to a zero pressure barostat during 20 ps. Finally, we cooled the sample during 0.2 ns at 300 K, which leads to a polycrystal with residual stress[49] as low as 10^{-5} GPa.

It is worth noting that usually, MD simulations employ a relaxation time of 0.2 ns for surfaces and nanoparticles; nevertheless, because the nanostructures we are analyzing present particular details in their geometry, it could be necessary to perform longer time relaxations. Hence, the structures are carried out at 300 K following a 1.0 ns temperature ramp, as was discussed previously by Reyes et al.[23] Thus, in the hope of ensuring an equilibrium condition, we maintained the simulation at 300 K, for 200 ns, hopping also that these long-time dynamics capture the grain boundary activity. The surface shrinkage was computed % $A = 100 \times (A_f - A_i)/A_i$, where A_f is the total hNP surface considering both inner and outer surfaces after a 200 ns dynamic and A_i is the surface before the hNP relaxation.

The atomic shear strain of the i-atom (η_i) was computed from the Von Mises shear invariant as follows

$$\eta_i = \sqrt{\eta_{yz}^2 + \eta_{xy}^2 + \eta_{xz}^2 + \frac{(\eta_{yy} - \eta_{xx})^2 + (\eta_{zz} - \eta_{yy})^2 + (\eta_{zz} - \eta_{xx})^2}{6}}$$

(1)

where subscripts correspond to the components of the strain tensor. The local shear strain[51,52] was originally proposed for viscoelastic or amorphous like solids. However, in crystalline materials, it has been shown to be a good descriptor.

The structure recognition, visualization, and postprocessing were performed employing the OVITO software.[53,54] Dislocation recognition was performed with the DXA algorithm, also implemented in the OVITO code.[54] A more detailed description of the crystalline structure was obtained with the Crystal Analysis Tool (CAT).[54] This code is a group of algorithms that, by means of several defect-recognition methods, create a unique signature for a particular group of atoms, and then the patterns are matched with the CAT database using graph maps.

■ RESULTS AND DISCUSSION

To address the stability of hNPs, Jiang et al.[24] proposed to follow the behavior of potential energy curves. The way that the curve drops helps to describe the failure modes qualitatively, classifying the systems as unstable if the hNP collapse in a conventional NP; stable if the hNP maintains its original structure; and half-stable if the nanostructure collapse but keeps its hollow structure. We note that a single-crystal hNP with constant potential energy is consistent with the fact that the hNP retains its initial structure without the nucleation of further defects. However, in hNPs with polycrystalline structures, the behavior is quite different; because of the preexistence of defects, the potential energy curves suffer several drops but not necessarily related to compaction or collapse of the whole nanostructure. Therefore, we consider a structure as stable if it can maintain its spherical shape, admitting a partial shrinkage not higher than a few surface steps, more strictly a surface variation not higher than 1%. Figure 1a shows two representative cases of stable and half-stable systems (see also Figure S1). As it is observed, the stable ones are characterized not only by the grain boundary structure but also for some isolated SF, which are the consequence of the polycrystalline relaxation; this behavior is evidenced in Figure 1b for the case t = 5 nm. During the first 40 ns, the hNP maintains its size but allow the grain boundary accommodation and surface reconstruction. On the other hand, in the half-stable system (t = 2 nm), the curve suffers several partial drops until 80 ns. Those events are related to the hNP shrinkage and sphericity loss, triggered by an intense grain boundary activity.

To explore how shell defects control the structural stability, we studied hNPs with different grain sizes. Figure 2a classify the stable to half-stable transition for several grain sizes and thicknesses. In all cases, we set the hNP diameter at 20 nm. From the figure, it is evident that stable to half-stable threshold do occur for smaller thickness values, with critical cases at t = 1.5 nm for crystalline and t = 2.0 nm for a grain size of d = 12 nm. We remark that both cases show slight differences; for instance, small dislocations embryos or defective hexagonal close-packed (hcp) planes are observed in d = 12 nm; we attributed them to the preexistence of defects during the polycrystal relaxation. In all the polycrystalline cases, there is evidence of reconstruction or SF propagation even if they are stable systems, as is shown in Figure 2b,c. This is expected
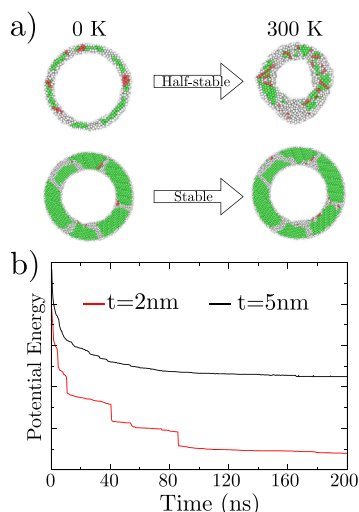
Figure 1. (a) Stable and half-stable representation of a hNP. The green and red atoms correspond to fcc and hcp crystalline structures, respectively. Atoms with non traditional close-packed structures are depicted in white. These atoms are used as a reference to illustrate the grain boundary region, and the inner and outer surfaces of the hNP. Both figures correspond to a cross-section of 1 nm thickness. (b) Potential energy for two different shell thicknesses (t), with 20 nm diameter, and a grain size of 10 nm. The potential energy is in arbitrary units.

because the grain boundary structure acts as a barrier for atomic slipping planes. On the other hand, it is remarkable that the stable single-crystal configurations do not present evidence of any defective atoms. However, the onset of the stable to half-stable transition shows the generation of SF in single-crystal spheres, which are a more invasive process as the slips travel almost freely along the whole structure.

For smaller d values, Figure 2 shows that thicker shells are required to stabilize hNPs, suggesting that highly defective shells are prone to collapse even at room temperatures. Even though our study is focused on room temperature conditions, higher temperatures can increase the grain boundary diffusion processes. Figure S2 shows that an increase of only 100 K can shift the transition from stable to half-stable, being more sensitive to collapse the hNP with higher grain boundary densities. To understand how the polycrystalline shell affects the structural stability, we can note that the grain boundary structure is often a route of hardening for polycrystalline systems.[55,56] However, at smaller grain sizes ($d \leq 10$ nm), the grain boundary acts as stress accumulation sites, favoring dislocations, and the fault mechanism associated. We note that our results are quite different from those observed in the literature.[24,28,29] For single-crystal Au hNPs, it is noticed that a shell thickness of a few lattice parameters is necessary to stabilize hNPs. In experiments, the obtained thicknesses of Au hNPs are far from those sizes,[38,57,58] suggesting that the preexistence of defects or grain boundaries might introduce an alternative mechanism for hNP instability and collapse. In this case, a shell softening is a direct consequence of a small grain size structure. To observe those mechanisms, Figure 3 displays shear strain maps of hNPs with different grain sizes; the figure establishes a comparison of initial and final configurations after a 200 ns dynamic. Although the hNP does not collapse, it is rather evident that the strain is localized in the grain boundary structure. For $d = 12$ nm, the shear is mainly localized in
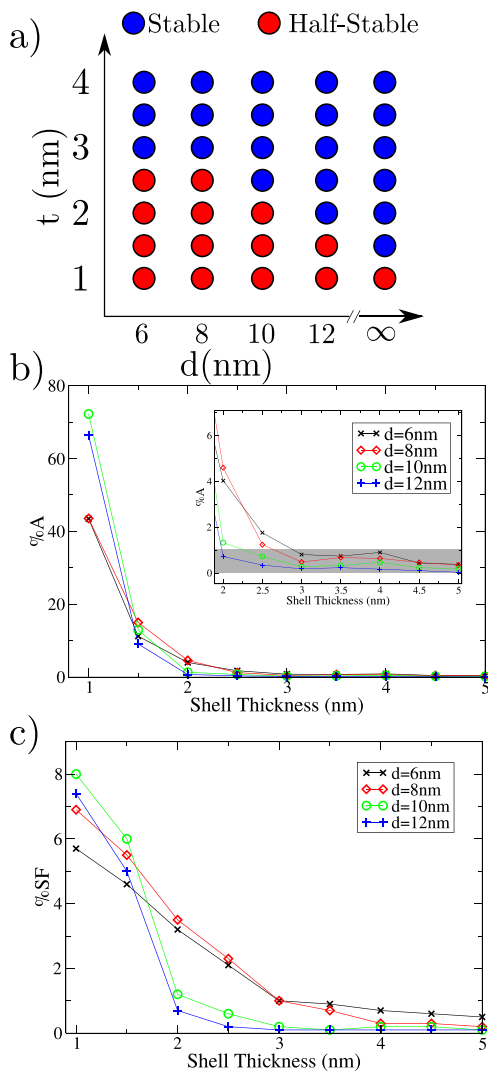

Figure 2. (a) Role of the grain size on the stability of a hNP of 20 nm diameter. Results are presented for different wall thickness t. Red and blue circles correspond to stable and half-stable configurations, respectively. The character ∞ corresponds to the crystalline case. (b) Surface area variation after a 300 K dynamic of 200.0 ns. Inset shows a zoom of the stable and half-stable region (gray). (c) SF formation as a thickness function is illustrated.

thinner fringes in the grain boundary zone. However, for $d = 6$ and $d = 8$ nm, these fringes transform into wider regions of highly localized shear strain. Besides, close to triple grain junctions, several amorphization zones are found.

The influence of grain size in shear is illustrated in Figure 4. In a relaxed polycrystalline bulk, almost no shear must be expected; however, the histograms reveal Gaussian distributions with similar centroids at strains near to 0.025. These shifts are attributed to the stress imposed by the cavity. We note that the centroids are similar for all structures, suggesting that this is a consequence of geometry instead of shell composition (pristine or polycrystalline). On the other hand, the most shear atoms on distributions tails are quite different. The histograms showed a significative increase of atoms with the high strain; in fact, the larger the grain size, the fast the decrease in the number of most shear atoms. The inverse relation between distribution tails and the grain boundary is consistent with that illustrated in strain maps.
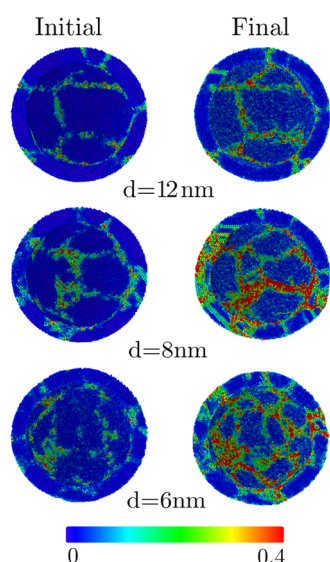
Initial   Final

d=12 nm

d=8 nm

d=6 nm

0   0.4

Figure 3. Shear strain of a hNP with 2 nm thickness and radius of 10 nm. Every snapshot represents the configuration before and after relaxation (200.0 ns).
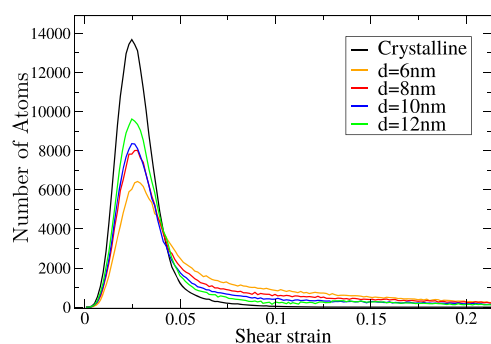

Figure 4. Shear strain histograms of a hNP with 10 nm radius and thickness of 5 nm. The shear strain was computed after 200 ns dynamics. Each curve was generated from a hNP with a different grain size. The black curve represents the single-crystal hNP case.

In single-crystal hNPs, the absence of defects implies that collapse or shrinkage starts from both inner or outer surfaces[21−23,27,42] mediated by slips of preferential planes that travel along with the whole structure. On polycrystalline case, as the grain boundary can act as a barrier for dislocation emitted from surfaces, the dominant mechanism for deformation or stress release can be found at the grain boundaries. Figure 5a shows the role displayed by grain boundary during the shrinkage of a hNP. Pointed in Figure 5a-ii by a blue arrow, the annihilation of the grain boundary region between two neighboring grains is shown; the same region is illustrated in Figure 5b employing a cross-section of the hNP. Both figures show that the grain boundary region is wholly reconstructed during the hNP dynamic. An outer view is illustrated in Figure 5c, where the color map highlights the rotation angle during the grain boundary accommodation. We note that sintering leads not only to the stress release but also the loss of sphericity and the compaction of the hNP. On the other hand, a similar grain boundary sintering is depicted by the black arrow; however, in that case, the grain boundary reconstruction is dominated by dislocation activity (see Figure S3), in particular, by Shockley partial dislocations and the subsequent twining formation Figure 5a-iii. In Figure 5a-iv, the
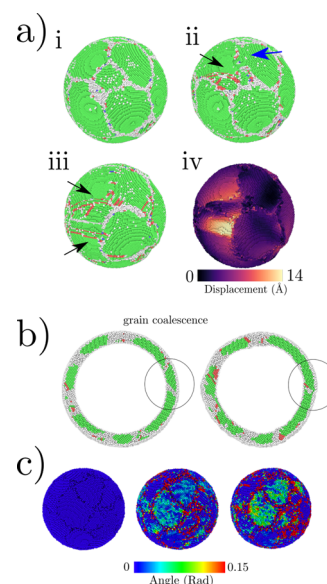

Figure 5. (a) Cross-section of a 1 nm thickness hNP. Atoms are colored by its local crystalline structure following a CNA analysis, (iv) displacement vectors relative to initial configuration. (b) Grain boundary region after the hNP relaxation (1 nm). The circle shows a region with grain coalescence after a 200 ns dynamic. (c) Angle variation of a hNP with respect to the initial configuration.

magnitude of the atomic displacements with respect to the initial configuration is shown; interestingly, twinning regions highlights as the most active zone for hNP compaction, with displacement fields greater than 1 nm.

Polycrystalline bulks employed in our simulations were extensively relaxed, ensuring the absence of grain boundary activity before the hNPs were created. Thus, the grain boundary mediated collapse seems to be driven as a consequence of the hNP geometry. In our case, the presence of cavity introduces the additional degree of freedom for grain boundary diffusion and accommodation, triggering the compaction or partial shrinkage of the hNP. Interestingly, this statement is in good agreement with experimental evidence,[7,9,59] which commonly shows a size decrease or irregular shapes once the template core is removed during the hNP synthesis.

■ CONCLUSIONS

The stability of polycrystalline Au hNPs was investigated through MD simulations. While shell thickness and radius are commonly referenced as the relevant parameters to character-ize hNPs,[15,20,22,24,26−30] the presented simulations allow us to conclude that the grain boundary structure also plays a dominant role in their structural stability. In particular, it was found an inverse dependence on the stable/half-stable transition with the grain size reduction. This behavior is attributed to the increase in potential failure sources at the grain boundaries, which are triggered by the stress introduced by the hollow design.

In contrast with theoretical reports studying the stable to half-stable threshold of single-crystal hNPs,[15,20,24,30] our results suggest that to achieve larger sizes, fewer defective shells are necessary. Additionally, we found that single-crystal hNPs are more stable in comparison with all the grain sizes studied here. Based on the MD evidence, it is noticed that single-crystal hNP half-stable transition is often attributed to surface effects

mediated by partial dislocations.[23,27] Interestingly, grain boundaries are often thought of as a strengthening mechanism in polycrystalline materials.[32,42] However, in hNPs, collapse could be introduced by grain sliding or by partial dislocations taking place from grain boundaries. In this aspect, polycrystalline structures are potential dislocation sources, increasing the probability of a partial collapse.

Our analysis shows how hNP compaction is dominated by a combination of grain diffusion, rotation, dislocation emission, and twining. These mechanisms are in good agreement with experimental evidence of the partial shrinkage after the hNP synthesis,[7,9,40,59] where size decrease or further shape modifications with respect to their templates could be a consequence of grain boundary activity driven by core removal.[15,60−62] Usually, experiments show the initial and the final picture of the synthesis processes, but where the resulting defects come from is still not understood. Atomistic simulations not only help us to show the mechanism but also to shed light on why those defects are generated. This is a relevant issue because knowing the exact mechanism that triggers the failures could help to improve experiments in order to achieve larger and thinner hNPs. In this way, grain boundary engineering or grain boundary doping has been shown as an alternative to modify grain boundary diffusion[63,64] or grain boundary strengthening;[65,66] both factors could be a determinant to delay or diminish grain boundary-assisted collapse.

While our contribution is focused on the role of polycrystalline domains, future works might look for larger channels or porous shells as the obtained by the Kirkendall effect or calcination technique.[59,67,68] In addition, temperature effects consistent with experimental conditions deserve to be included.[30] Finally, although our study considers Au systems, we expect that the techniques and qualitative results presented here can be extended to other polycrystalline materials.

■ ASSOCIATED CONTENT

Ⓢ Supporting Information

The Supporting Information is available free of charge at https://pubs.acs.org/doi/10.1021/acs.jpcc.0c00258.

Potential energy curves, temperature effects, and dislocation identification (PDF)

■ AUTHOR INFORMATION

Corresponding Author

Felipe J. Valencia − Centro de Investigación DAiTA Lab, Facultad de Estudios Interdisciplinarios, Universidad Mayor, Santiago 7560913, Chile; Centro para el Desarrollo de la Nanociencia y la Nanotecnología, CEDENNA, Santiago 9170124, Chile; ⓞ orcid.org/0000-0002-5461-6885; Email: felipe.valenciad@gmail.com

Authors

Max Ramírez − Departamento de Física, Facultad de Ciencias, Universidad de Chile, Santiago 7800024, Chile; Centro para el Desarrollo de la Nanociencia y la Nanotecnología, CEDENNA, Santiago 9170124, Chile

Alejandro Varas − Departamento de Física, Facultad de Ciencias, Universidad de Chile, Santiago 7800024, Chile; Centro para el Desarrollo de la Nanociencia y la Nanotecnología, CEDENNA, Santiago 9170124, Chile

José Rogan − Departamento de Física, Facultad de Ciencias, Universidad de Chile, Santiago 7800024, Chile; Centro para el Desarrollo de la Nanociencia y la Nanotecnología, CEDENNA, Santiago 9170124, Chile

Complete contact information is available at:
https://pubs.acs.org/10.1021/acs.jpcc.0c00258

Notes

The authors declare no competing financial interest.

■ ACKNOWLEDGMENTS

■ REFERENCES

(1) Liang, H.-P.; Zhang, H.-M.; Hu, J.-S.; Guo, Y.-G.; Wan, L.-J.; Bai, C.-L. Pt hollow nanospheres: facile synthesis and enhanced electrocatalysts. Angew. Chem., Int. Ed. 2004, 43, 1540−1543.

(2) Zhang, J. Z. Biomedical applications of shape-controlled plasmonic nanostructures: a case study of hollow gold nanospheres for photothermal ablation therapy of cancer. J. Phys. Chem. Lett. 2010, 1, 686−695.

(3) Mahmoud, M. A.; O'Neil, D.; El-Sayed, M. A. Hollow and Solid Metallic Nanoparticles in Sensing and in Nanocatalysis. Chem. Mater. 2014, 26, 44−58.

(4) Yang, Z.; Xu, F.; Zhang, W.; Mei, Z.; Pei, B.; Zhu, X. Controllable preparation of multishelled NiO hollow nanospheres via layer-by-layer self-assembly for supercapacitor application. J. Power Sources 2014, 246, 24−31.

(5) Shervani, S.; Mukherjee, P.; Gupta, A.; Mishra, G.; Illath, K.; Ajithkumar, T. G.; Sivakumar, S.; Sen, P.; Balani, K.; Subramaniam, A. Multi-mode hydrogen storage in nanocontainers. Int. J. Hydrogen Energy 2017, 42, 24256−24262.

(6) Lou, X. W.; Archer, L. A.; Yang, Z. Hollow micro-/nanostructures: Synthesis and applications. Adv. Mater. 2008, 20, 3987−4019.

(7) Fan, H. J.; Gösele, U.; Zacharias, M. Formation of nanotubes and hollow nanoparticles based on Kirkendall and diffusion processes: a review. Small 2007, 3, 1660−1671.

(8) Sen, R.; Govindaraj, A.; Suenaga, K.; Suzuki, S.; Kataura, H.; Iijima, S.; Achiba, Y. Encapsulated and hollow closed-cage structures of WS2 and MoS2 prepared by laser ablation at 450-1050°C. Chem. Phys. Lett. 2001, 340, 242−248.

(9) Zhang, Q.; Wang, W.; Goebl, J.; Yin, Y. Self-templated synthesis of hollow nanostructures. Nano Today 2009, 4, 494−507.

(10) Ras, R. H. A.; Kemell, M.; de Wit, J.; Ritala, M.; ten Brinke, G.; Leskelä, M.; Ikkala, O. Hollow inorganic nanospheres and nanotubes with tunable wall thicknesses by atomic layer deposition on self-assembled polymeric templates. Adv. Mater. 2007, 19, 102−106.

(11) Joo, J. B.; Zhang, Q.; Lee, I.; Dahl, M.; Zaera, F.; Yin, Y. Mesoporous anatase titania hollow nanostructures though silica-protected calcination. Adv. Funct. Mater. 2012, 22, 166−174.

(12) Zheng, G.; Lee, S. W.; Liang, Z.; Lee, H.-W.; Yan, K.; Yao, H.; Wang, H.; Li, W.; Chu, S.; Cui, Y. Interconnected hollow carbon nanospheres for stable lithium metal anodes. Nat. Nanotechnol. 2014, 9, 618.

(13) Koo, B.; Xiong, H.; Slater, M. D.; Prakapenka, V. B.; Balasubramanian, M.; Podsiadlo, P.; Johnson, C. S.; Rajh, T.;

Shevchenko, E. V. Hollow iron oxide nanoparticles for application in lithium ion batteries. *Nano Lett.* **2012**, *12*, 2429−2435.

(14) Zhang, L.; D'Acunzi, M.; Kappl, M.; Auernhammer, G. K.; Vollmer, D.; van Kats, C. M.; van Blaaderen, A. Hollow silica spheres: synthesis and mechanical properties. *Langmuir* **2009**, *25*, 2711−2717.

(15) Shan, A.; Chen, Z.; Li, B.; Chen, C.; Wang, R. Monodispersed, ultrathin NiPt hollow nanospheres with tunable diameter and composition via a green chemical synthesis. *J. Mater. Chem. A* **2015**, *3*, 1031−1036.

(16) Cheng, D.; Zhou, X.; Xia, H.; Chan, H. S. O. Novel method for the preparation of polymeric hollow nanospheres containing silver cores with different sizes. *Chem. Mater.* **2005**, *17*, 3578−3581.

(17) Dai, Y.; Jiang, H.; Hu, Y.; Fu, Y.; Li, C. Controlled synthesis of ultrathin hollow mesoporous carbon nanospheres for supercapacitor applications. *Ind. Eng. Chem. Res.* **2014**, *53*, 3125−3130.

(18) Ma, F.-X.; Hu, H.; Wu, H. B.; Xu, C.-Y.; Xu, Z.; Zhen, L.; David Lou, X. W. Formation of Uniform Fe3O4 Hollow Spheres Organized by Ultrathin Nanosheets and Their Excellent Lithium Storage Properties. *Adv. Mater.* **2015**, *27*, 4097−4101.

(19) Tianou, H.; Wang, W.; Yang, X.; Cao, Z.; Kuang, Q.; Wang, Z.; Shan, Z.; Jin, M.; Yin, Y. Inflating hollow nanocrystals through a repeated Kirkendall cavitation process. *Nat. Commun.* **2017**, *8*, 1261.

(20) Valencia, F. J.; González, R. I.; Tramontina, D.; Rogan, J.; Valdivia, J. A.; Kiwi, M.; Bringa, E. M. Hydrogen Storage in Palladium Hollow Nanoparticles. *J. Phys. Chem. C* **2016**, *120*, 23836−23841.

(21) Yang, L.; Bian, J. J.; Zhang, H.; Niu, X. R.; Wang, G. F. Size-dependent deformation mechanisms in hollow silicon nanoparticles. *AIP Adv.* **2015**, *5*, 077162.

(22) Valencia, F. J.; González, R. I.; Vega, H.; Ruestes, C.; Rogan, J.; Valdivia, J. A.; Bringa, E. M.; Kiwi, M. Mechanical Properties Obtained by Indentation of Hollow Pd Nanoparticles. *J. Phys. Chem. C* **2018**, *122*, 25035−25042.

(23) Reyes, P. N.; Valencia, F. J.; Vega, H.; Ruestes, C.; Rogan, J.; Valdivia, J. A.; Kiwi, M. The stability of hollow nanoparticles and the simulation temperature ramp. *Inorg. Chem. Front.* **2018**, *5*, 1139−1144.

(24) Jiang, L.; Yin, X.; Zhao, J.; Liu, H.; Liu, Y.; Wang, F.; Zhu, J.; Boey, F.; Zhang, H. Theoretical investigation on the thermal stability of hollow gold nanoparticles. *J. Phys. Chem. C* **2009**, *113*, 20193−20197.

(25) Akbarzadeh, H.; Abbaspour, M.; Mehrjouei, E.; Ramezanzadeh, S. Ag−Au nanoparticles encapsulated inside porous hollow carbon nanospheres: a molecular dynamics study. *New J. Chem.* **2018**, *42*, 13619−13628.

(26) Akbarzadeh, H.; Mehrjouei, E.; Shamkhali, A. N.; Abbaspour, M.; Salemi, S.; Ramezanzadeh, S. Au@void@AgAu Yolk-Shell Nanoparticles with Dominant Strain Effects: A Molecular Dynamics Simulation. *J. Phys. Chem. Lett.* **2017**, *8*, 5064−5068.

(27) Huang, R.; Shao, G.-F.; Zeng, X.-M.; Wen, Y.-H. Diverse melting modes and structural collapse of hollow bimetallic core-shell nanoparticles: A perspective from molecular dynamics simulations. *Sci. Rep.* **2015**, *4*, 7051.

(28) Senturk Dalgic, S. Size Dependent Properties of Hollow Gold Nanoparticles: A Theoretical Investigation. *Acta Phys. Pol., A* **2016**, *129*, 531−534.

(29) Jiang, L.; Sun, W.; Gao, Y.; Zhao, J. Geometric thermal phase diagrams for studying the thermal dynamic stability of hollow gold nanoballs at different temperatures. *Phys. Chem. Chem. Phys.* **2014**, *16*, 6623−6629.

(30) Jiang, S.; Zhang, Y.; Gan, Y.; Chen, Z.; Peng, H. Molecular dynamics study of neck growth in laser sintering of hollow silver nanoparticles with different heating rates. *J. Phys. D: Appl. Phys.* **2013**, *46*, 335302.

(31) Yu, J.; Yu, X. Hydrothermal synthesis and photocatalytic activity of zinc oxide hollow spheres. *Environ. Sci. Technol.* **2008**, *42*, 4902−4907.

(32) Shan, Z. W.; Adesso, G.; Cabot, A.; Sherburne, M. P.; Syed Asif, S. A.; Warren, O. L.; Chrzan, D. C.; Minor, A. M.; Alivisatos, A. P. Ultrahigh stress and strain in hierarchically structured hollow nanoparticles. *Nat. Mater.* **2008**, *7*, 947−952.

(33) Yan, Z.; Bao, R.; Huang, Y.; Chrisey, D. B. Hollow particles formed on laser-induced bubbles by excimer laser ablation of Al in liquid. *J. Phys. Chem. C* **2010**, *114*, 11370−11374.

(34) Yan, Z.; Bao, R.; Chrisey, D. B. Excimer laser ablation of a Pt target in water: the observation of hollow particles. *Nanotechnology* **2010**, *21*, 145609.

(35) Mahmoud, M. A.; Garlyyev, B.; El-Sayed, M. A. Controlling the catalytic efficiency on the surface of hollow gold nanoparticles by introducing an inner thin layer of platinum or palladium. *J. Phys. Chem. Lett.* **2014**, *5*, 4088−4094.

(36) Newhouse, R. J.; Wang, H.; Hensel, J. K.; Wheeler, D. A.; Zou, S.; Zhang, J. Z. Coherent vibrational oscillations of hollow gold nanospheres. *J. Phys. Chem. Lett.* **2011**, *2*, 228−235.

(37) Liang, H.-P.; Wan, L.-J.; Bai, C.-L.; Jiang, L. Gold hollow nanospheres: tunable surface plasmon resonance controlled by interior-cavity sizes. *J. Phys. Chem. B* **2005**, *109*, 7795−7800.

(38) Zhang, K.; Holloway, T.; Wingfield, A.; Pradhan, J.; Cao, W.; Pradhan, A. K. Hollow gold nanospheres: growth morphology, composition and absorption characteristics. *Mater. Res. Soc. Symp. Proc.* **2011**, *3*, 76−82.

(39) Preciado-Flores, S.; Wang, D.; Wheeler, D. A.; Newhouse, R.; Hensel, J. K.; Schwartzberg, A.; Wang, L.; Zhu, J.; Barboza-Flores, M.; Zhang, J. Z. Highly reproducible synthesis of hollow gold nanospheres with near infrared surface plasmon absorption using PVP as stabilizing agent. *J. Mater. Chem.* **2011**, *21*, 2344−2350.

(40) Schwartzberg, A. M.; Olson, T. Y.; Talley, C. E.; Zhang, J. Z. Synthesis, Characterization, and Tunable Optical Properties of Hollow Gold Nanospheres. *J. Phys. Chem. B* **2006**, *110*, 19935−19944.

(41) Ibáñez, M.; Fan, J.; Li, W.; Cadavid, D.; Nafria, R.; Carrete, A.; Cabot, A. Means and limits of control of the shell parameters in hollow nanoparticles obtained by the Kirkendall effect. *Chem. Mater.* **2011**, *23*, 3095−3104.

(42) Valencia, F. J.; Pinto, B.; Kiwi, M.; Ruestes, C. J.; Bringa, E. M.; Rogan, J. Nanoindentation of polycrystalline Pd hollow nanoparticles: Grain size role. *Comput. Mater. Sci.* **2020**, *179*, 109642.

(43) Plimpton, S. Fast Parallel Algorithms for Short-Range Molecular Dynamics. *J. Comput. Phys.* **1995**, *117*, 1−19.

(44) Daw, M. S.; Baskes, M. I. Embedded-atom method: Derivation and application to impurities, surfaces, and other defects in metals. *Phys. Rev. B: Condens. Matter Mater. Phys.* **1984**, *29*, 6443.

(45) Sheng, H. W.; Kramer, M. J.; Cadien, A.; Fujita, T.; Chen, M. W. Highly optimized embedded-atom-method potentials for fourteen fcc metals. *Phys. Rev. B: Condens. Matter Mater. Phys.* **2011**, *83*, 134118.

(46) Simmons, G. *Single Crystal Elastic Constants and Calculated Aggregate Properties*; Southern Methodist University Press, 1965.

(47) Lee, B.-J.; Shim, J.-H.; Baskes, M. Semiempirical atomic potentials for the fcc metals Cu, Ag, Au, Ni, Pd, Pt, Al, and Pb based on first and second nearest-neighbor modified embedded atom method. *Phys. Rev. B: Condens. Matter Mater. Phys.* **2003**, *68*, 144112.

(48) Grochola, G.; Russo, S. P.; Snook, I. K. On fitting a gold embedded atom method potential using the force matching method. *J. Chem. Phys.* **2005**, *123*, 204719.

(49) Valencia, F.; Mella, J. D.; González, R. I.; Kiwi, M.; Bringa, E. M. Confinement effects in irradiation of nanocrystalline diamond. *Carbon* **2015**, *93*, 458−464.

(50) Valencia, F. J.; González, R. I.; Valdivia, J. A.; Kiwi, M.; Bringa, E. M.; Rogan, J. Inducing Porosity on Hollow Nanoparticles by Hypervelocity Impacts. *J. Phys. Chem. C* **2017**, *121*, 17856−17861.

(51) Falk, M. L.; Langer, J. S. Dynamics of viscoplastic deformation in amorphous solids. *Phys. Rev. E: Stat. Phys., Plasmas, Fluids, Relat. Interdisc. Top.* **1998**, *57*, 7192.

(52) Shimizu, F.; Ogata, S.; Li, J. Theory of shear banding in metallic glasses and molecular dynamics calculations. *Mater. Trans.* **2007**, *48*, 2923−2927.

(53) Stukowski, A. Visualization and analysis of atomistic simulation data with OVITO-the Open Visualization Tool. *Modell. Simul. Mater. Sci. Eng.* **2010**, *18*, 015012.

(54) Stukowski, A. Structure identification methods for atomistic simulations of crystalline materials. *Modell. Simul. Mater. Sci. Eng.* **2012**, *20*, 045021.

(55) Hansen, N. Hall-Petch relation and boundary strengthening. *Scr. Mater.* **2004**, *51*, 801−806.

(56) Weertman, J. R. Hall-Petch strengthening in nanocrystalline metals. *Mater. Sci. Eng., A* **1993**, *166*, 161−167.

(57) You, J.; Zhang, G.; Li, C. Exceptionally high payload of doxorubicin in hollow gold nanospheres for near-infrared light-triggered drug release. *ACS Nano* **2010**, *4*, 1033−1041.

(58) Tuersun, P.; Han, X. e. Optical absorption analysis and optimization of gold nanoshells. *Appl. Opt.* **2013**, *52*, 1325−1329.

(59) Chang, S. L. Y.; Barnard, A. S.; Dwyer, C.; Hansen, T. W.; Wagner, J. B.; Dunin-Borkowski, R. E.; Weyland, M.; Konishi, H.; Xu, H. Stability of porous platinum nanoparticles: Combined in situ TEM and theoretical study. *J. Phys. Chem. Lett.* **2012**, *3*, 1106−1110.

(60) Peng, Z.; You, H.; Wu, J.; Yang, H. Electrochemical synthesis and catalytic property of sub-10 nm platinum cubic nanoboxes. *Nano Lett.* **2010**, *10*, 1492−1496.

(61) Hong, J. W.; Kang, S. W.; Choi, B.-S.; Kim, D.; Lee, S. B.; Han, S. W. Controlled Synthesis of Pd-Pt Alloy Hollow Nanostructures with Enhanced Catalytic Activities for Oxygen Reduction. *ACS Nano* **2012**, *6*, 2410−2419.

(62) Xia, X.; Wang, Y.; Ruditskiy, A.; Xia, Y. 25th Anniversary Article: Galvanic replacement: a simple and versatile route to hollow nanostructures with tunable and well-controlled properties. *Adv. Mater.* **2013**, *25*, 6313−6333.

(63) Nakagawa, T.; Sakaguchi, I.; Shibata, N.; Matsunaga, K.; Mizoguchi, T.; Yamamoto, T.; Haneda, H.; Ikuhara, Y. Yttrium doping effect on oxygen grain boundary diffusion in α-Al2O3. *Acta Mater.* **2007**, *55*, 6627−6633.

(64) Stubican, V.; Osenbach, J. Influence of anisotropy and doping on grain boundary diffusion in oxide systems. *Solid State Ionics* **1984**, *12*, 375−381.

(65) Özerinç, S.; Tai, K.; Vo, N. Q.; Bellon, P.; Averback, R. S.; King, W. P. Grain boundary doping strengthens nanocrystalline copper alloys. *Scr. Mater.* **2012**, *67*, 720−723.

(66) Ikuhara, Y.; Yoshida, H.; Sakuma, T. Impurity effects on grain boundary strength in structural ceramics. *Mater. Sci. Eng., A* **2001**, *319−321*, 24−30.

(67) Yang, J.; Lind, J. U.; Trogler, W. C. Synthesis of hollow silica and titania nanospheres. *Chem. Mater.* **2008**, *20*, 2875−2877.

(68) Tang, Y.; Chen, S.; Mu, S.; Chen, T.; Qiao, Y.; Yu, S.; Gao, F. Synthesis of capsule-like porous hollow nanonickel cobalt sulfides via cation exchange based on the Kirkendall effect for high-performance supercapacitors. *ACS Appl. Mater. Interfaces* **2016**, *8*, 9721−9732.